LAWRENCE
LIVERMORE
NATIONAL
LABORATORY

LLNL-JRNL-768521

Inspection of plate weldments through an interposed layer of viscoelastic material using an elastic-electromagnetic scanning method

K. Fisher, O. Mayes, D. Obenauff, P. Haugen

February 28, 2019

Journal of the Acoustical Society of America

Disclaimer

Inspection of plate weldments through an interposed layer of viscoelastic material using an elastic-electromagnetic imaging method

Karl A. Fisher
Lawrence Livermore National Laboratory, L-333
7000 E. Avenue, Livermore, CA, 94551,
fisher34@llnl.gov

Owen Mays
Lawrence Livermore National Laboratory, L-xxx
7000 E. Avenue, Livermore, CA, 94551,
mays8@llnl.gov

Peter Haugen
Lawrence Livermore National Laboratory, L-184
7000 E. Avenue, Livermore, CA, 94551,
haugen2@llnl.gov

David Obenauf
Lawrence Livermore National Laboratory, L-xxx
7000 E. Avenue, Livermore, CA, 94551,
obenauf2@llnl.gov

Short title: Inspection of plate weldments

LLNL-JRNL-768521

Abstract

Development of improved approaches in the nondestructive evaluation of welds in coated steel plates for naval structures continues to be an area of interest for the Department of Defense, (DoD) and the military complex. In this article we will investigate an elastic-microwave based detection and imaging method that can inspect welds and the plate surface with the coating in place. The evaluation was performed on two test articles that were designed to represent critical structural components with flaws of interest. The flaws, cracks and weld defects have been included in the test articles to determine detection sensitivity and accuracy of the proposed method. Our approach uses a microwave interferometer (MI) operating at 94 GHz to record the scattered response of the surface of a steel plated as it is driven by an incident elastic field. The MI can "see" (penetrate) through the viscoelastic coating to the upper surface of the plate. Out-of-plane displacement amplitudes of 10nm in the frequency range (10kHz to 35kHz) are readily observable, with the key feature being that the surface bond between the coating and the steel plate is undisturbed. The non-contact aspect of the interferometer allows for large surface regions to be accurately and efficiently scanned in space and time. These spatiotemporal data coupled with specialized wavefield processing algorithms provide powerful detection and imaging capabilities. From these wavefield data sets, a plate thickness mapping capability has been demonstrated that can detect thickness changes on the order of 0.79 mm (1/32 in.) with spatial resolution on the order of the spatial sampling rate, 7.5 mm (~1/4 in.). We have also shown that a topological energy analysis of the wavefield data can detect and locate small flaws, on the order of 5-10 mm (0.19-0.40 in.) in the welded joint of a 1.5" thick T-plate. Note, all of these results are obtained *through* a 50.8 mm (2 in.) thick viscoelastic coating without disturbing the coating or the coating bond. The current results indicate that we are detecting and locating damage (flaws) in the plate that are significantly smaller than the wavelength of the propagating guided modes (λ ~ 200 mm). Classical scattering theory places a ($\lambda/2$) resolution limit on the detectability of flaws in terms of the incident wavefield, however, since the spatial discretization of the surface region is much smaller, $\Delta l_x = \Delta l_y = 15$mm, and with the inherent natural focusing of the time reversal operation, we are able to detect smaller flaws on the order of $\Delta l/3$ ~ 5mm. It is important to realize that we are not imaging the flaw but detecting and localizing a difference between a simulated reference (pristine) sample and the measured (damaged) sample, relative to a spatial grid on the surface. At present the algorithm cannot resolve individual flaws within a grid space just their cumulative effect. Even with the current limitations, this detection approach appears to be a promising alternative to traditional phased array imaging methods where the coating layer must be removed prior to inspection.

PACS numbers: 43.60.Pt, 43.60.Ac, 43.35.Zc

I. INTRODUCTION

Development of improved approaches in the nondestructive evaluation of welded steel plates for large structures continues to be an area of interest for the DoD and the military complex. Numerous technologies with similar degrees of technical maturity are currently available to inspection and maintenance efforts. These include, but are not limited to, ultrasonic testing using phase array technology, digital and film radiography, dye penetrant, optical-visual and eddy current methods. [1,2] With the exception of radiography, some form of mechanical contact or direct line of sight is required at the surface of the plate for these methods to be effective. If the plate is coated with an insulating layer and or a viscoelastic coating, direct access to the surface of the plate is compromised and the resulting effect on imaging and flaw detection performance can be significantly degraded. Current working solutions involve removing some or all of the coating in the neighborhood of the weld seam. Removal of the coating is expensive, time consuming and has the potential to adversely alter the structural integrity of the surrounding coating and the bond with the underlying steel plate. Practical alternatives to removing the coating necessitate the ability interrogate the underlying plate structure with the coating in place. In this investigation we will explore an approach that utilizes a microwave interferometer (MI) to measure the dynamic response of the steel plate through the viscoelastic coating as it is excited (driven) by guided acoustic modes propagating in the plate.

Guided acoustic modes possess two characteristics that make them ideal for this particular inspection problem. The first is, they can propagate in the plate structure efficiently across large distances with minimal signal attenuation. The second, is that depending on the mode, they can be 'tuned' to interact with different types of flaws in the plate.[3] The microwave interferometer can record the total out-of-plane displacement of the plate due to these propagating modes. Since the viscoelastic coating is a non-conductive, low dielectric constant material it is essentially transparent to electromagnetic radiation and has a negligible effect on the displacement sensitivity of the MI. Established methods using acoustic wavefield imaging (AWI) can then be applied to the recorded data for damage detection and flaw localization.[4,5]

In this article, we report on an elastic-microwave based detection and imaging method for coated plate weldments. The evaluation is performed on two test articles that are designed to represent key structural components with features of interest. Details of the materials and simplified mechanical drawings are given for the test articles. Flaws and cracks are included in the weld seams to characterize detection sensitivity and location accuracy of the proposed method. In the following sections we present the theoretical concepts associated with this detection scheme. Beginning with an idealized description of the detection process, we describe the key measurement parameters and theory. A simplified description of the interferometer and associated electronics to measure and record the surface displacements is given. Wavefield imaging techniques require the data to be acquired uniformly in space and in time. Accurately capturing the response of propagating modes in the plate plays a critical role in the detection and location of flaws or damage. Choosing optimal excitation signal parameters to facilitate these measurements is also discussed, along with a calibration

using a commercial laser vibrometer. A 3D time-domain finite element solver will be used to define measurement parameters and provide the forward model for the adjoint imaging approaches that are presented in subsequent sections [6]. The small physical size and basic construction of the test articles is such that the entire system can be effectively modeled using simple boundary conditions and desktop computational resources. Flaw locations determined through the imaging process are compared against the actual flaw locations in the test articles. Finally, a discussion of the results and a path forward for future developments will conclude this article.

II. EXPERIMENTAL SYSTEM

A. Elastic-electromagnetic flaw detection

Consider an elastic wave propagating in a coated steel plate. Here, the goal is to inspect the plate and weld structure without damaging or compromising the structural integrity of the viscoelastic coating layer. The plate is considered as a waveguide, with preferential bias to guided modes that satisfy the dispersion relation from the corresponding boundary conditions.[7] Modes can be chosen that maximize detection sensitivity for either surface defects, or internal defects of the plate. [8] Deviations in the plate thickness can also alter the dispersion characteristics of the waveguide, preventing some modes from propagating and enhancing others. Modes can also be selected to accommodate specific spatial sampling requirements for wavefield analysis. Another characteristic of guided modes that is attractive for this application is they can be tailored to be sensitive to changes at the boundaries or the center of the plate. The natural focusing of energy of the wave guide allow for very efficient propagation over large distances within the structure. This feature offers the capability of inspecting large regions under the viscoelastic coating with minimal intrusion.

Damage in the plate can alter a propagating mode in several ways, such as changing its direction (reflection), mode conversion, and or attenuation. Defects such as cracks and voids tend to cause reflections and can be inferred from the presents of a scattered wavefield. As the propagating modes interact with damage and flaws in the plate, the total displacement field is a superposition of the incident, scattered and evanescent wave fields. Depending upon the size of the flaw with respect to the incident wavelength, the scattered field can be minimal. Scanning the entire region, improves the detectability of small flaws by bringing the measurement system closer to the source of the scattered field as depicted in Fig 1.0.

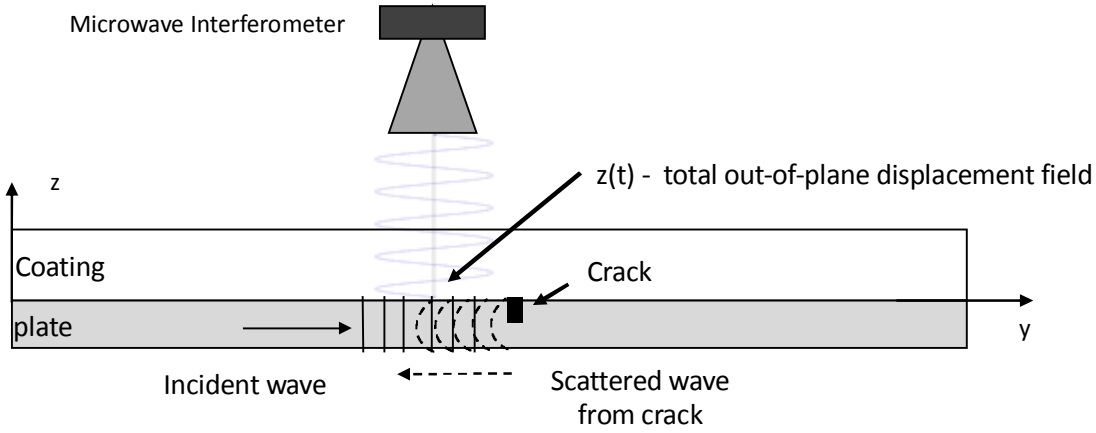

FIG. 1. Elastic-microwave interferometric based measurement approach. Here the interferometer measures the total out-of-plane displacement on the upper surface of the plate. Flaws will generate localized changes in the elastic field due to propagating and non-propagating modes.

B. Microwave interferometric sensing

Interferometric measurements have a long history of utility in the areas of remote sensing, material characterization, biology, motion detection and astronomy. [9] Typically, these methods fall in the optical regime as the cost effectiveness and availability of precision coherent light sources is continually improving. Similar approaches using lower frequency EM radiation in the 10's to 100's of GHz have also been developed for situations where optical approaches are not practical. [10] Theory and design of these systems has been explored and reported in the literature. [11,12]

The operational principle for the interferometer is based on a phase comparison between a *reference* signal, represented as $A_1(t) = A_1 \cos(\omega t)$, and a *received signal* given as

$$A_2(t) = A_2 \cos\left(\omega t + 2\pi(D + w(t))/\lambda\right) \quad (1)$$

The received signal in Eq 1. is a combination of the reference signal and two additional phase terms, a constant phase term, that corresponds to the total path length, D, and a time varying phase term, proportional to the out-of-plane displacement of the plate w(t). The microwave carrier wavelength is

λ. Following the development outlined in Ref. [12], we generate two separate quadrature signals by multiplying the received signal $A_2(t)$ by a reference signal $A_1\cos(\omega t)$, and a 90 degree shifted reference signal $A_1\cos(\omega t + \pi/2)$. A low pass filter is then applied to the product of $A_1\cos(\omega t)*A_2(t)$ to remove the 2ω component. The resulting in-phase term is

$$\mathrm{I(t)} = \tfrac{1}{2}\mathrm{A_1A_2cos(2\pi D/\lambda)} - \tfrac{1}{2}\mathrm{A_1A_2\,sin(2\pi D/\lambda)w(t)}\,, \tag{2}$$

and the quadrature term, obtained by low pass filtering the product $A_1\cos(\omega t + \pi/2)*A_2(t)$ results in

$$\mathrm{Q(t)} = \tfrac{1}{2}\mathrm{A_1A_2sin(2\pi D/\lambda)} - \tfrac{1}{2}\mathrm{A_1A_2\,cos(2\pi D/\lambda)w(t)} \tag{3}$$

The assumption, $\lambda \gg |\,w(t)|$ has been used to simplify the analysis and is both a necessary condition and a practical consideration based on amplitude limits of the out of plane displacements $w(t)$ (i.e. nanometer range). The MI wavelength λ is 3 mm. We note that the first terms in Eqs. 2 and 3 are *time-independent* (DC) while the second terms are *time-dependent* (AC). Since the excitation signals are known *a priori*, we can determine the out-of-plane displacement, w(t), by combining AC and DC components of Eqs. 2 and 3 in the following manner

$$w(t) = \left(\frac{\lambda}{2\pi}\right)\left[\frac{\mathrm{I_{DC}Q_{AC} + I_{AC}Q_{DC}}}{\mathrm{I_{DC}}^2 + \mathrm{Q_{DC}}^2}\right] \tag{4}$$

Experimentally, the DC and AC components are determined by low or high pass filter operation on the quadrature signals I(t) and Q(t) based on the spectral content of the excitation signal.

The basic design for the 94 GHz microwave interferometer (MI) is shown in Fig. 2. The phase change is tracked through the use of a quadrature mixing circuit which generates two voltage signals each proportional to the surface displacement. The two quadrature signals designated as I(t) and Q(t), are low pass filtered (LPF) and amplified with a low noise amplifier (LNA) before being digitized and recorded for post-processing.

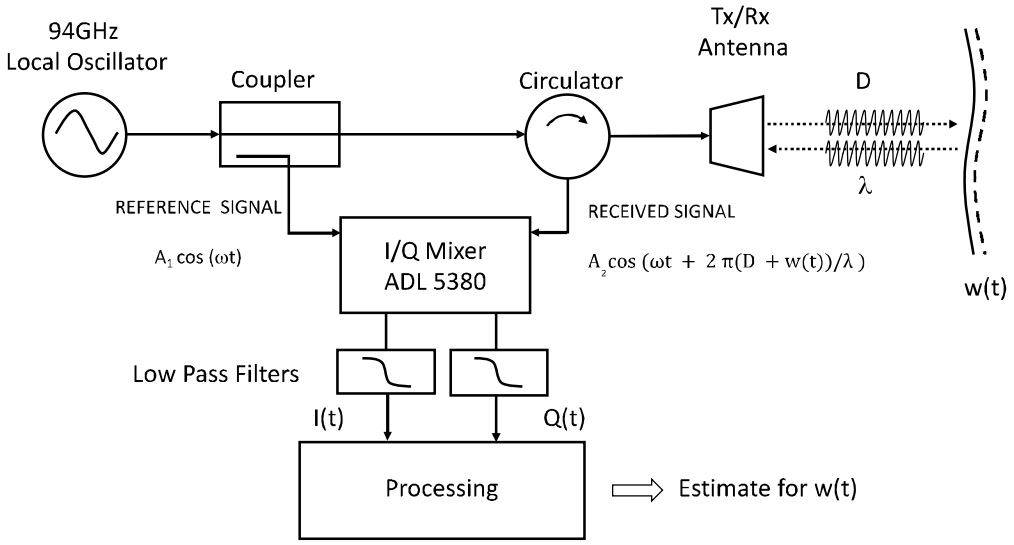

FIG. 2. Basic operational components of the W-Band homodyne Microwave Interferometer (reflectometer). Here, w(t) is the time-varying acoustic surface displacement, D is the standoff path length, λ is the wavelength of the transmitted signal. Reference and received signals are mixed to produce the in-phase and quadrature results I(t) and Q(t) respectively. The quadrature signals are processed and combined to obtain an estimate of w(t) given by Eq. 4.

The interferometer system is a combination of a commercial front end (Millitech) and a custom I & Q mixing and sampling backend (Analog Devices, ADL-5380). The transceiver horn antenna has dimensions of 25mm x 25mm x 100mm. The modest size and weight of the interferometer allows the system to be easily configured to conduct spatial scanning for elastic wavefield analysis. The current system can easily transmit through several inches of urethane or other rubberized low dielectric polymers. The system has a moderate surface offset and illumination region. Since the MI system does not make physical contact with the structure, large regions can be scanned accurately with minimalcontact requirements.

C. Coated plate weldments

The test surrogates for the hull structural components are fabricated from A36 carbon steel plates. Two designs are chosen to evaluate different weld conditions and inspection geometries. The first surrogate is a planar geometry with a double V butt weld along the center. The nominal dimensions are 50.8 mm thick, by 304.8 mm wide by 457.2 mm in length. The second surrogate is a T-joint with double V butt welds. The plate and the rib are each 304.8 mm by 304.8 mm square. The

thickness of the plate is 38.1 mm and the thickness of the rib is 25.4 mm. For both surrogate components, the weld material is ER706-6, 7018/7024. A 50.8 mm layer of polyether polyurethane is then molded on to the upper surface of each plate surrogate. Details of these plates are shown in a later section.

Various surface defects are milled into the upper surface of the plates to introduce thickness variations to simulate corrosion thinning. Flaws and cracks have been incorporated into the weldments to simulate expected defects. The size and location of these features is designed to exercise the detection and location sensitivities of the proposed technique.

Handbook values for the properties of steel are stated to be: Young's Modulus E = 20 GPa, Poisson's ratio v = 0.28, and the density p = 7800 kg/m^3. Nominal material properties for the polyurethane layer are given as: Young's Modulus E = 0.4 GPa, Poisson's ratio v = 0.49, and the density p = 1040 kg/m^3. These are general values used to calculate the dispersion relations of the plate and in the finite element model to simulate the transient wave-propagation.

D. Experimental setup and measurement process

Figure 3 illustrates the scanning setup for the coated steel plates. The 50.8 mm. coating on the upper surface has been omitted for clarity. A Wilcoxon F-7 piezoelectric shaker provides an excitation signal on the upper surface of the plate through means of a ¼-20 threaded rod passing through the coating and threaded onto the upper surface of the plate. The actuator is located on the centerline of the plate, approximately 228.6 mm from the weldment. The microwave interferometer, which is comprised of the microwave circuit and directional horn antenna, is mounted in a standard 4-space lab rack enclosure with the waveguide mounted on the front panel directed downward. The rack is attached to a fixture which allowed the enclosure to be mounted to the spindle of a Bridgeport vertical mill.

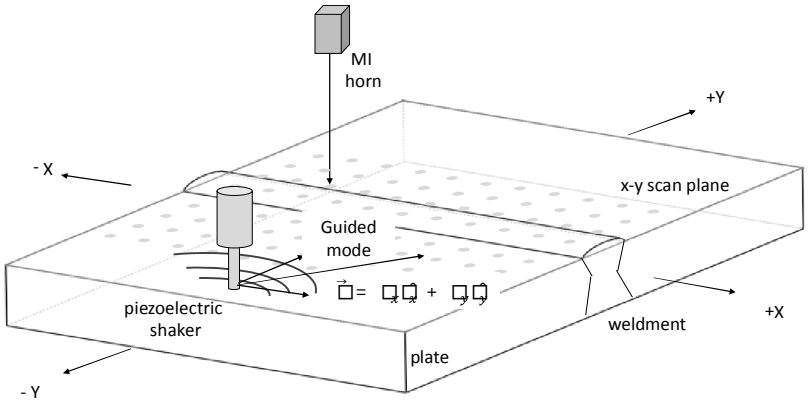

FIG. 3. Scanning set up for the coated steel plates. The 2 in. coating on the upper surface has been omitted for clarity. The microwave interferometer (MI) is held stationary in the spindle of a vertical machine mill. The plate is positioned under the horn at each of the scan locations (gray dots) by adjusting the x-y travel on the mill bed. The guided modes in the plate are generated by a piezoelectric shaker driven by a sinusoidal windowed pulse.

The welded plate is then positioned horizontally on the mill table with the coating side facing upward. A thin ¼ inch thick rubber sheet is used to isolate the plate from the mill bed. In this approach, the microwave interferometer is stationary, and the heavy plates are moved relative to the horn position. The mill provides a convenient environment with the appropriate mechanical leverage to support the heavy coated plates. The mill also can maintain positional accuracy and repeatability (with the aid of a digital read out) on the order of +/- 0.002mm.[13] The inherent rigidity of the mill isolates the interferometer from motion induced vibration and positional variation resulting in very stable and consistent scanning platform. Using the digital readouts of the mill, a 2D array of scan locations can be recorded using the x-y travel dials on the mill bed.

A 5-cycle 21kHz windowed sinusoidal pulse provides the drive signal to the shaker. The pulse is generated using an Agilent 33210 signal generator and then amplified to 800 V pk-pk using a Wilcoxon power amplifier model no. PA8HF, and a Wilcoxon matching transformer model no. N7FS. The repetition rate of the drive pulse is approximately 6Hz (100ms) this provides a sufficient delay between consecutive pulses to minimize generation of standing waves in the plate. At this frequency, only the S_o and A_o modes are excited, the corresponding wavelengths, are λ_{So} = 255mm, λ_{Ao} = 125mm.[3] Spatial sampling for the shortest wave length, $\lambda_{Ao}/8$, gives spatial grid $\Delta x=\Delta Y$ = 15mm. The resulting spatial array is size is n_x = 11 and n_y = 12. The interferometer is positioned to a specified location (x_i,y_i,h) above the plate and records the out-of-plane displacement. The data window for the measurement is synchronized with the shaker signal and is the same duration as the drive repetition (100 ms). The windowed data is digitized and averaged to improve the signal-to-noise ratio (SNR). The recorded waveforms are organized into 3D spatiotemporal data sets w(x, y, t). Elastic wavefield images are then obtained by taking 2D slices at specific instances of time, (t_n ; n = 1,N) where N is the number of sample intervals in the time window. Figure 4 illustrates a typical 1D scan data set. The image on the left shows the test plate prior to application of coating (flaws and weld exposed/visible for clarity). The interferometer measurement points are in red and the shaker excitation location is in green. The source location is held constant for all measurements on the plates. The plot on the right shows the out-of-plane displacements as a function of time for each highlighted scan location (i =1, 12). The data has been preprocessed by bandpass filtering, normalization, and DC offset removal.

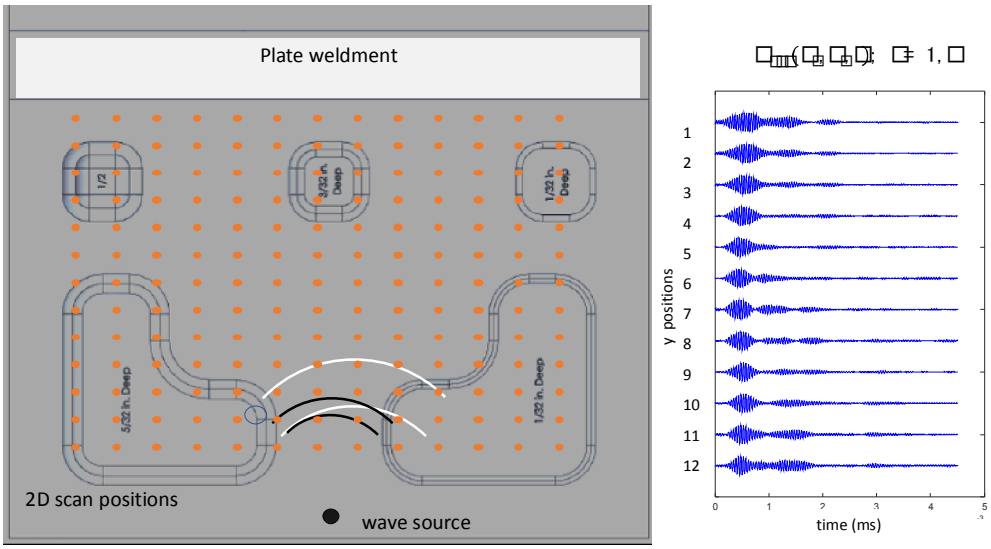

FIG. 4. The array plot on the right is a typical 1D wavefield data set with waveform amplitudes normalized. The shaker source location (black) is constant for all scan locations (red). The displacement measurements are recorded through the coating. The outlines show the details of the five thinned regions, each has a different depth and edge profile.

In a separate set of measurements on the reverse side (uncoated), the microwave interferometer was calibrated against a commercial laser vibrometer (Polytech model PM-40). The measured amplitude of the out-of-plane surface displacements of the steel plate was determined to be $|w_{tot}| \sim 7$ nm.

III. ACOUSTIC WAVEFIELD IMAGING AND ANALYSIS

Acoustic wavefield imaging (AWI) offers a powerful approach to determining the condition of a component or structure before and after damage. The AWI method utilizes spatiotemporal data sets recorded at discrete regular intervals across the surface of the structure. Data taken in this manner provides a wealth of information regarding space and time changes of propagating waves as they interact with inspected structure. Methods such as frequency-wavenumber analysis [4,5], topological energy methods [14,15,16,17], diffuse field imaging [18] and spectral techniques[19, 20] can only be realized with accurate spatiotemporal data sets of the elastic field. In the next two sections, we will investigate the capabilities of the elastic microwave interferometric approach for surface characterization and detection of weld flaws. Two approaches will now be examined to assess the capabilities of the

acousto-electromagnetic scanning technique: (1) corrosion thinning and (2), flaw localization in the weldments.

A. Detecting corrosion thinning in plates using a localized wavenumber estimate

The spatial and temporal periodicities of the wavefield can be reconstructed from the information obtained from the spatiotemporal data scans of the surface of the plate. Following the development in Ref. [4], let us consider the total out-of-plane displacement, *w*, at the surface of the plate as a superposition of incident and scattered wave fields, then

$$w_{tot}(x,y,t) \ = w_{inc}(x,y,t) \ + \ w_{scat}(x,y,t) \tag{5}$$

Or in terms of a harmonic wave,

$$w_{tot}(x,y,t) \ = A_{inc}e^{i(\vec{k}\cdot\vec{r}-\omega t)} \ + \ \mathcal{R}A_{inc}e^{i(\vec{k}\cdot(\vec{r}-\vec{r}_s)-\omega t)} \tag{6}$$

Where $\vec{r} \ = \ x\hat{e}_x \ + \ y\hat{e}_y \ and \ \vec{r}_s \ = \ x_s\hat{e}_x \ + \ y_s\hat{e}_y$ are position vectors and $\mathcal{R}$ is a coefficient relating the scattered wave amplitude to the incident amplitude, A_{inc}. The spatial wavenumber is, $\vec{k} \ = \ k_x\hat{e}_x \ + \ k_y\hat{e}_y$ with $k_x = \frac{w}{c_o}cos\theta_o \ \ and \ \ k_y = \frac{w}{c_o}sin\theta_o$. The total surface displacement can be represented in the frequency wavenumber space by applying a three-dimensional Fourier transform

$$\widehat{w}_{tot}(k_x,k_y,\omega) = \mathcal{F}_{3D}\{w_{tot}(x,y,t)\}$$

$$= \iiint_{+\infty}^{+\infty} w_{tot}(x,y,t)e^{i(k_x x+ \ k_y y-\omega t)}dx \ dy \ dt \tag{7}$$

Where in the frequency-wavenumber space, the incident and scattered wavefields are similarly defined as Eq. 5.

$$\widehat{w}_{tot}(k_x,k_y,\omega) \ = \widehat{w}_{inc}(k_x,k_y,\omega) \ + \ \widehat{w}_{scat}(k_x,k_y,\omega) \tag{8}$$

Representing the data in this manner offers a powerful approach to analyzing complicated displacements on the surface of the plates.

For this analysis, we apply acoustic wavefield imaging techniques to characterize regions of plate thinning (i.e., loss of thickness). Plate thinning occurs due to corrosion of the metal surface at the metal-coating interface. The corrosion at the interface between plate and the coating undermines the structural integrity of the bond which may lead to bond failure and possible detachment. For this study, the flat 50.8mm. thick plate had a number of regions milled down to various depths and shapes to simulate corrosion defects of interest. The entire plate surface was then covered with the viscoelastic layer. It should be noted that the simulated corrosion defects were entirely filled during the coating process. In actuality, such defects would be filled with air, water, or other corrosion byproducts. The region of interest was scanned as shown in Fig. 5 and a three-dimensional data set (2 spatial, one temporal) was recorded of the out-of-plane data. The experimental data set is given as

$$w^E(x_i, y_j, \mathrm{t}) \text{ for all } \mathrm{S}(x_i, y_j) \; and \; (0 \leq t \; < T) \tag{9}$$

Here, the set of spatial locations $\mathrm{S}(x_i, y_j)$ are on the upper surface of the plate and the time window is (0<t<T). The duration of the data, T, is chosen to be long enough such that the any total elastic field is approaching a quiescent level before the next excitation pulse is generated. For our experiment this was approximately 100ms.

The wavenumber analysis is based on a method presented by Behboodian [21]. The basic idea is that propagating guided modes are sensitive to changes in the plate thickness. The corresponding wavenumbers will exhibit similar localized sensitivities. These sensitivities are a result of the dispersive nature of the modes as depicted in standard plots, where the phase velocity, c_{ph}, for a given mode is plotted relative to a frequency-thickness product *fd* [3]. Therefore, at a constant frequency, f_o, thickness variations d(x,y), in the plate will result in changes in the phase velocity. The local wavenumber $k^{local}(x_i, y_j)$ is then related to the frequency divided by the phase speed $k^{local} = 2\pi f/c_{ph} = \omega/c_{ph}$. Hence, localized estimates for the surface wavenumbers provide a direct indication of the local thickness of the plate. We will now present an approach to calculate these localized wavenumber estimates from the spatiotemporal data sets.

In this processing approach we begin by transforming the 3D data from time to frequency $\widehat{w}^E(x,y,\omega)$ by applying a Fourier transform to obtain,

$$\widehat{w}^E(x, y, \omega) = \mathcal{F}_{1D}\{w^E(x, y, \mathrm{t})\} \tag{10}$$

where $\mathcal{F}_{1D}$ denotes a 1D version of Eq. 7 with respect to t. We then select a 2D spatial slice of the data at a frequency in the bandwidth of the filtered data, which for this analysis was f_o = 21 kHz , $\omega_o = 2\pi f_o$. A region of interest, $\widetilde{w}^E_{tukey}(x_i, y_j, \omega_o)$, $i = 1,..,N_x, j = 1,..,N_y$ in this time slice is selected and a 2D tapered cosine (Tukey) window is then applied,

$$\widetilde{w}^E_{tukey}(x_i, y_j, \omega_o) = T_{2D}\{\widehat{w}^E(x_i, y_j, \omega_o)\} \tag{11}$$

This windowed subset is the input for the next step where we apply a spatial-spatial frequency analysis of a moving 3x3 window centered at each scan location $\mathcal{F}_{2D}\{\widetilde{w}^E_{tukey}(x_i, y_j, \omega_o)\}$. The location where the maximum value of the absolute value of the Fourier transform occurs is an estimate of the dominant wavenumber in that region.

$$k'(x_i, y_j, \omega_o) \sim \max\left|\widetilde{w}^E_{tukey}\left(x_i, y_j, \omega_o\right)\right| \tag{12}$$

The process is illustrated in Fig. 5.

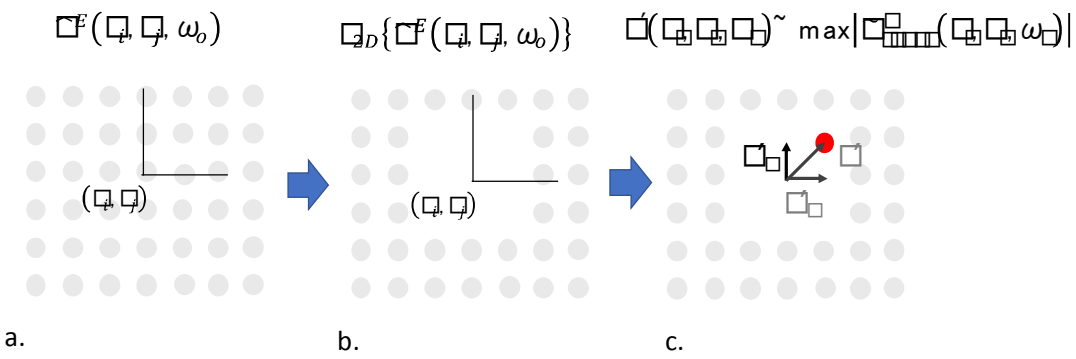

Figure 5. Process of determining a local wavenumber estimate from a region of interest (roi) subset. **a.** A slice of the spato-temporal $\widehat{w}^E$ data is chosen at ω_o. **b**. A 3x3 region centered at (x,y) is selected and a 2D spatial transform is calculated. **c.** The maximum absolute value of a 2D spatial transform in the 3x3 widow centered at (x_i,y_i) is proportional to an estimate of the local wavenumber $k'(x_i,y_i,\omega_o)$. The wavenumber estimate is repeated at each scan location using the selected region of interest.

For the 3x3 region of interest shown, the local wavenumber has two components (+/- k_x, +/-k_y), only the +k_y will be considered in this analysis. From the localized wavenumber estimate we can calculate a localize phase speed by dividing the frequency by the wavenumber estimate

$$c_{ph}^{o}(x_i, y_j, \omega_o) = \omega_o / k'_{ph}(x_i, y_j, \omega_o) \quad (13)$$

The complexity of the elastic field in the finite plate geometry precludes the ability to isolate dispersive effects of single modes. The wavenumber estimate described above will have contributions from several different propagating modes. There is however a region on the group velocity dispersion curves at *fd* ~ 2.0, where the three propagating modes share a common 'approximate' group velocity, this is highlighted in Fig. 6.a. In this region, the group velocity for the A0 mode is insensitive to changes in the frequency-thickness product *fd*. On either side of this group velocity locus, the S0 and A1 modes change rapidly with *fd*. Similar sensitivity changes to *fd* are present in the phase velocity dispersion curves (highlighted in Fig. 6.b) where the A_O and S_O modes exhibits less sensitivity to changes in the frequency-thickness product at *fd* ~2 than A_1. The common group velocity at this locus supports the assertion that some energy for

all three modes will be in present at each grid location, $S(x_i, y_j)$, and that differencing techniques using a small perturbation can be applied to isolate strong dispersion sensitivities.

The process is as follows. We will assume that the nominal plate thickness, *d*, is constant at 50.8mm. The frequency-thickness product fd at the locus where the group velocities of the three propagating modes are equal is $(fd)_0$~ 2.03 (Fig. 6.a). This in turn, defines a *phase* speed, $c_{ph}^{0}(x_i, y_j, (fd)_0)$ from Fig. 6b. A second phase velocity, $c_{ph}^{1}(x_i, y_j, (fd)_1)$ is chosen, where $(fd)_1 = (fd)_o + \Delta(fd)$ and $\Delta(fd)$ is a small perturbation from $(fd)_o$. A differencing approach between c_{ph}^{o} and c_{ph}^{1} can be used to indicate regions on the plate where thickness changes are present using the following rational. In Figure 6.d we see that c_{ph}^{o} decreases with increasing $\Delta(fd)$. One can estimate differences in phase velocities along the dispersion curves due to plate thinning, by always choosing a perturbation in *frequency* such that $f_1 > f_o$ and noting that all of the perturbations in the *thickness* must follow the constraint that $d_1 < d_o$ (thinning of the plate). By limiting the perturbation to satisfy

$$f_o(d_o - d_1) > d_o(f_o - f_1) \quad (14)$$

then for all regions on the plate where the local thickness of the plate is d_o, $c_{ph}^{0} > c_{ph}^{1}$. Conversely, in regions where the plate is thinner (i.e., $d_0 > d_1$) the perturbed phase velocity will shift to the left with $c_{ph}^{1} > c_{ph}^{0}$. It is now possible to define a difference map, $\Phi(x_i, y_j)$, of the phase velocities across the scanned region as

$$\Phi(x_i, y_j) = c_{ph}^{0}(x_i, y_j, (fd)_0) - c_{ph}^{1}(x_i, y_j, (fd)_1) = \begin{cases} > 0, & d_o \\ < 0, & d_o > d_1 \end{cases} \quad (15)$$

Where $(fd)_1 = (fd)_0 + \Delta(fd)$, and $\Delta(fd)$ is a small perturbation of the frequency-thickness product. Thus, sign changes of $\Phi(x_i, y_j)$,can be used to infer regions of plate thinning relative to the nominal thickness d_o.

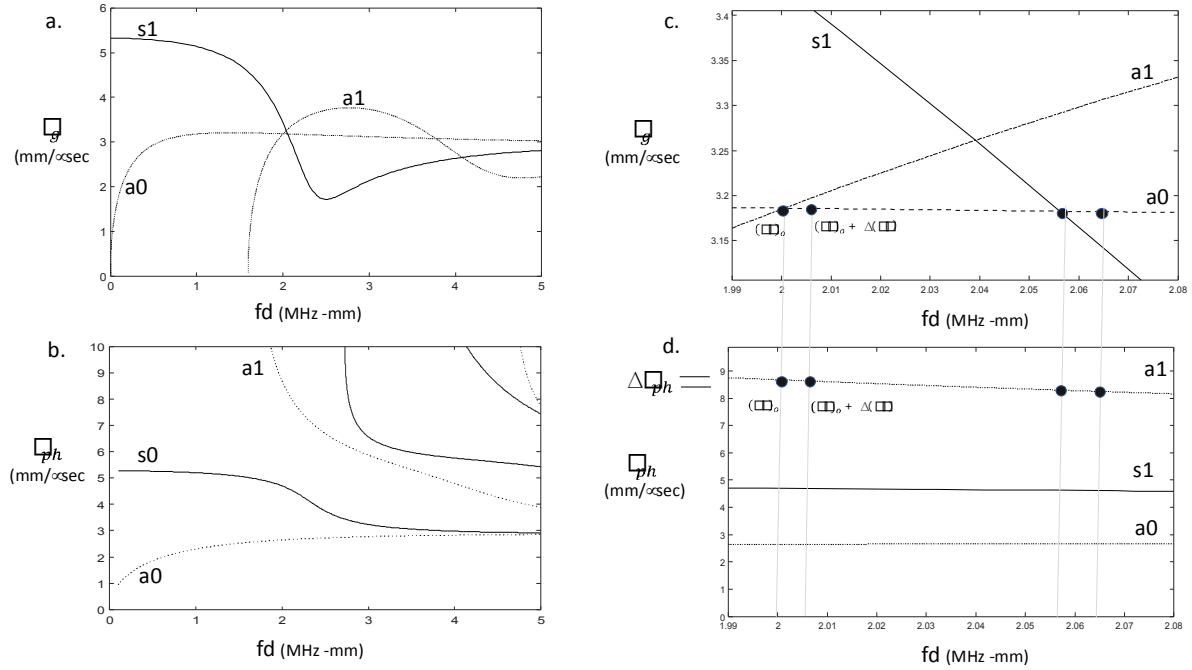

FIG. 6. The shaded region in Fig. 6a and 6b contains the locus of common group velocities that can be utilized to guide the differencing operations on the phase velocities. All things being equal, differences in phase velocity indicate thickness variations. Figures 6c and 6d are the expanded views of the highlighted region. Here the perturbed phase speed is calculated by $c_{ph}^{1}(x_i, y_j, (fd)_1)$; $(fd)_1 = (fd)_o + \Delta(fd)$ where $(fd)_o$ is the chosen at the locus of common group velocities and $\Delta(fd)$ is a small perturbation from the locus.

The processing approach is now applied to two different *fd* products of the experimental data. The first operational point chosen is *fd* = 1.99, where f_0 = 35.0 kHz and the nominal plate thickness is d_0 = 50.8 mm. Figure 7.a. shows the details of the imaged region of the upper surface of the coated plate and the location of the thinned regions. The data is processed following the method given above and the results are shown in Fig. 7.b. The image depicts a map of $\bar{\Phi}(x_i, y_j)$,

where, the thinnest region of the plate has been normalized to unity. Darker regions correspond to less thinning with black corresponding to no thinning. The depth of the thinned regions ranges from 0.78mm to 12.5mm. The 12.5 mm (½ in.) deep region in the upper left is clearly visible, as is the center region at 2.38 mm (3/32 in.) both show a significant difference from the non-thinned regions of the plate. The large black region in the center is indicating no little or no thinning which is consistent with the drawing of the plate. The two 'L-shaped' regions could not be resolved, and there are some inaccuracies with the actual locations of the thinned areas. These errors may be due in-part to the low-resolution sampling of the surface and to complications associated with mode conversion at the boundaries of the test plate.

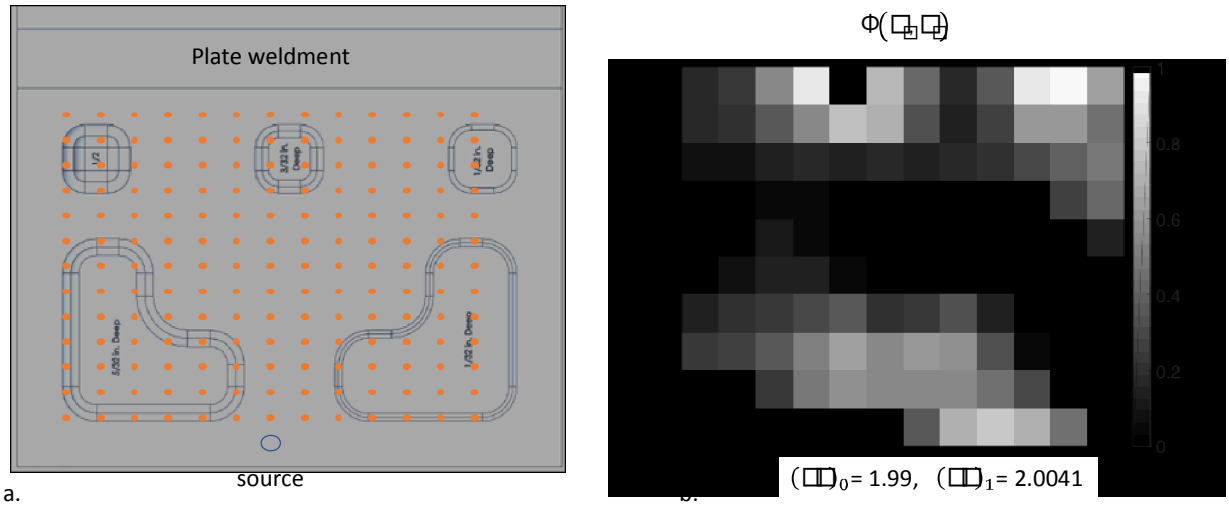

FIG. 7. In this example Fig. 7a. shows the scanned region of the plate and the thinned regions. The depth of the thinned regions ranges from 0.87mm to 12.5 mm (1/32 to ½ in.). Figure 7b shows a normalized version of Eq. 15 as applied to the scanned data. Here, the thinnest region of the plate (largest deviation from nominal) has been normalized to unity. Darker regions correspond to less thinning with black corresponding to no thinning. The 12.5 mm (½ in.) deep region in the upper left is clearly visible, as is the center region at 2.38mm (3/32 in.) both show a significant difference from the non-thinned regions of the plate. Note, the coating has been omitted for clarity in the image on the left.

A second locus was then selected to explore the consistency of the imaging approach. For this processing, the operational point was chosen at fd = 2.064, with f_0 = 35.0 kHz and the nominal plate thickness is d_0 = 50.8 mm. These results are shown in Fig. 8. As before, the thinnest region of the plate has been normalized to unity. Darker regions correspond to less thinning with black corresponding to no thinning. At this operational point, the algorithm provides similar results with possibly less artifacts in the

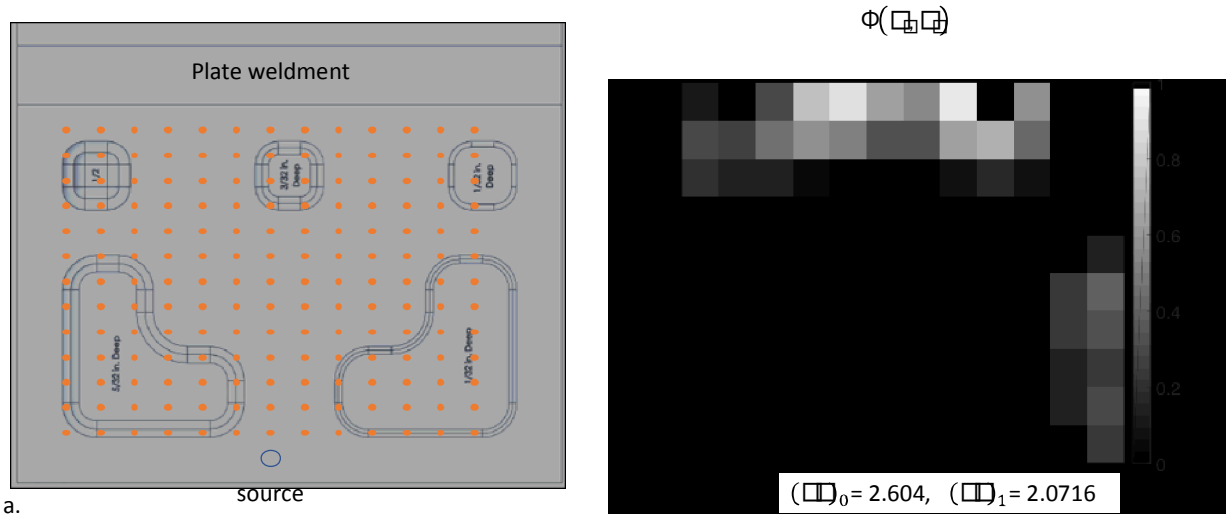

FIG. 8. For this processing, the operational point was chosen at fd = 2.064, with f_0 = 35.0 kHz and again, nominal plate thickness is d_0 = 50.8 mm. Similar results showing some of the thinned regions are obtained as found in Fig. 7., however, here the there are some slight indications of the backward 'L' shape. As before the resolution is low due to the coarse spatial sampling.

In the previous two examples, thickness variations were detected and imaged through the coating using a localized estimate for the phase speed. Even with the limitations introduced by the low spatial sampling, useful information in terms of a spatial map indicating thickness differences as a function of spatial position is obtained. Overall, some of the thinned regions near the weld bead are being detected while the large 'L-shaped' regions near the shaker are not being detected. It has been established in the literature that a certain amount of propagation distance is required for the guided modes to develop. For the current test plates, significant nearfield effects from the source may be corrupting the analysis and hindering the ability to image regions closer than half of the length of the plate. It is presumed that the complexity of the sound field will be significantly reduced in larger plate structures as a result of much longer propagation distances from the source to the scanned region. Larger plate structures will also have minimal edge effects and reduced mode conversions at plate boundaries. In the next section we will show that flaws, an order of magnitude smaller can be detected and localized using coarse wavefield data sets and a topological imaging method.

B. Crack detection in plate weldments using a topological energy method

In this section we will investigate a topological imaging method using an energy approximation to detect and localize cracks in plate weldments. The topological energy approach is derived from shape optimization techniques. Let us consider a cost function $\eta(\vec{x})$ that is defined as the difference between a reference field, w_o, and a *measured* field, w_m. If the two fields are identical, $(i.e., w_o = w_m)$ then the cost function is zero, $\eta(\vec{x}) = 0$, if however, the two fields are different $(w_o \neq w_m)$ then $\eta(\vec{x}) > 0$. Topological shape optimization seeks out a function g(**x**), that when combined with the reference field, minimizes the cost function $\min\{\eta(\vec{x})\}$ between the two fields. The function, $g(\vec{x})$, is defined as topological gradient that guarantees a decreasing $\eta(\vec{x})$. The nature of this function is such that regions of difference are highly localized in the field space, thus creating a powerful imaging algorithm for defect localization and detection.[8]

With acoustic wavefield data sets, the topological gradient $g(\vec{x})$, evaluates the misfit at each location (x_i,y_i) in the scanned region between the out-of-plane displacements for the *measured* field, w_m and the *pristine* field, w_o. Normally, the minimization problem is solved through an iterative process, where the gradient converges toward a solution that minimizes the cost function[15]. However, for NDE applications, the detection and location of flaws can be accomplished with a single iteration[4]. Dominguez[22], presents an approximate form of the topological gradient, $G_o(x,y)$, as a product of the energies of the *forward* and *adjoint* fields integrated over time

$$G_o(x,y) = \int_0^T \|w_o(x,y,t)\|^2 \|v_o(x,y,t)\|^2 dt \tag{16}$$

with

$$v_o(x,y,t) = w_m(x,y,T-t) - w_o(x,y,T-t) \tag{17}$$

Here, $w_o(x,y,t)$ is the out-of-plane surface response of the pristine plate (commonly referred to as the *forward* model). The adjoint field, $v_o(x,y,t)$, is the *backpropagated* difference between the pristine response and the response of the plate *after* damage has occurred. The subtlety in Eqs. 16 and 17 is that the causal arguments for the integral from [0,T], require v_o ,which is defined from [T , 0] to be reversed in time (i.e., $v_o(x,y,-t) = w_m(x,y,t) - w_o(x,y,t)$) before the integral can be solved. Implementation of the integral is straight forward, the pristine field, $w_o(x,y,t)$, can be obtained from experimental measurements or from a finite element model of the pristine system.

Experimental measurements on a pristine structure were unavailable for this study, so a 3D finite element model was developed to generate the damage-free wavefield data. The governing equation for the propagation of elastic waves in an elastic homogeneous medium is represented as[23]

$$\rho \frac{\partial^2 \vec{u}}{\partial t^2} - \nabla \cdot (c\nabla \vec{u}) = f \tag{18}$$

Where $\vec{u} = [u\ v\ w]$ is the displacement field, ρ is the density, c is an elastic tensor, and *f* are external body forces. The solution for the system described by Eq. 18 was obtained using a 3D transient finite element package.[24] The calculated surface displacements from the model will be used as the pristine structure response, $w_o(x, y, t)$.

Measurements of the damaged field, $w_m(x, y, t)$, are obtained experimentally during routine service and maintenance inspections. Peaks in the integral Eq. 16, occur at locations where the pristine field and the adjoint field are co-located in space and time. It is interesting to note that Behboodian presents a similar method using time-of-flight arguments.[21] The energy term calculated in Eq. 16 is a highly focused map of the local field differences (flaws) between a pristine part and a damaged part. From an optimization point of view, we realize that the natural refocusing of the time reversal operation will prevent the solution from converging to a local minimum, and thus, non-physical solutions are avoided [17].

In this experiment, we are inspecting a coated plate with a T-joint attached to the uncoated side. Figure 9 shows the plate geometry and the location of the 2D scan region on the surface of the plate. Several weld flaws of various sizes have been embedded into the weld for testing the approach. In this plate, there are no large thinned regions representing corrosion. The T-plate is slightly larger than the flat plate, and is constructed using two square plates 16” x 16” x 1.5” thick. The welded region is a vee to plate weldment on sides of the rib. Flaws and locations are shown in the Fig. 10a. As before, the shaker was attached to the upper surface of the plate through the coating. A similar measurement set up was used on the mill to facilitate recording the wavefield data. Recall that the interferometer is measuring the out-of-plane surface displacement of the plate due to the excitation signal from the shaker. Note, as before, the displacements are measured *through* the viscoelastic coating.

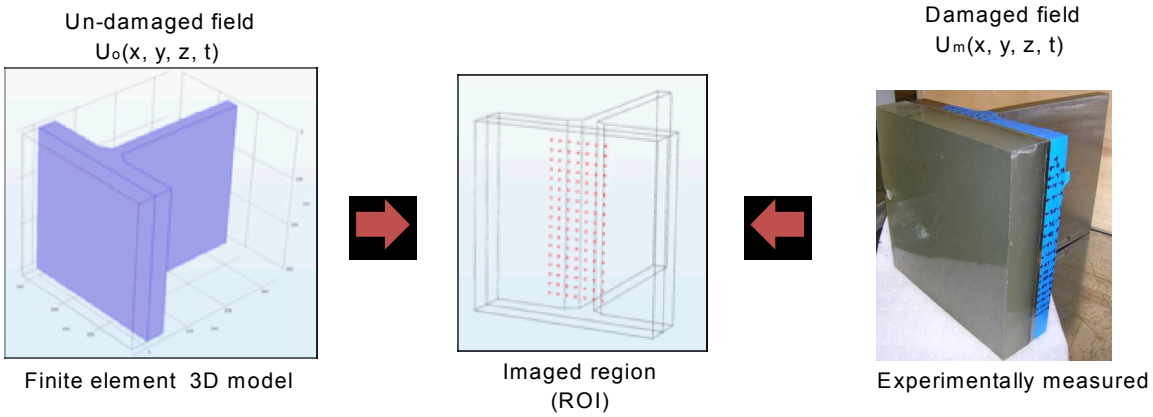

FIG. 9. Process for determining flaws in weldments using a topological energy method, the pristine data $u_o(x, y, z_o, t)$ is determined from a 3D finite element time domain model and the adjoint field $v_o(x, y, z_o, t)$ is determined from the time-reversed *difference* between the pristine model and experimental measurements.

The imaging results for the topological energy gradient, $G_0(x_i, y_j)$ are shown in Fig. 10b. The scan map on the left shows the locations of the wavefield data set (surface measurement locations, red circles, source location is green. Here, the scanned region of interest (ROI) has been chosen to cover the T-joint weldment and part of the surrounding plate. The contour map of $G_0(x_i, y_j)$, on the right clearly shows peaks at the locations of two of the reported flaws in the plate. The gradient map is showing the locations in the scan region where there are significant differences between the pristine coated T-plate model and the test article with the embedded flaws. Flaw #4 is 10mm and located in the heat affected zone (HAZ) of the rib weldment. Flaw #2 is a root crack in the base weldment of the T-plate, approximately 5mm in size. Note, that the excitation wavelength,λ, in the plate is approximately 110 mm (a0 mode at 21kHz) which is significantly larger than the flaws. The current results indicate that we are detecting and locating damage (flaws) in the plate that are significantly smaller than the wavelength of the propagating guided modes (λ_{a1} ~ 200 mm). Classical scattering theory places a (λ/2) resolution limit on the detectability of flaws in terms of the incident wavefield[22], however, since the spatial discretization of the surface region is much smaller, $\Delta l_x = \Delta l_y$=15mm, and with the inherent natural focusing of the time reversal operation, we are able to detect smaller flaws on the order of $\Delta l/3$ ~ 5mm. It is important to realize that we are not imaging the flaw but detecting and localizing a difference between a simulated reference (pristine) sample and the measured (damaged) sample, relative to a spatial grid on the surface. At present the algorithm cannot resolve individual flaws within a grid space just their cumulative effect. Even with the current limitations, this detection approach appears to be a promising alternative to traditional phased array imaging methods where the coating layer must be removed prior to inspection.

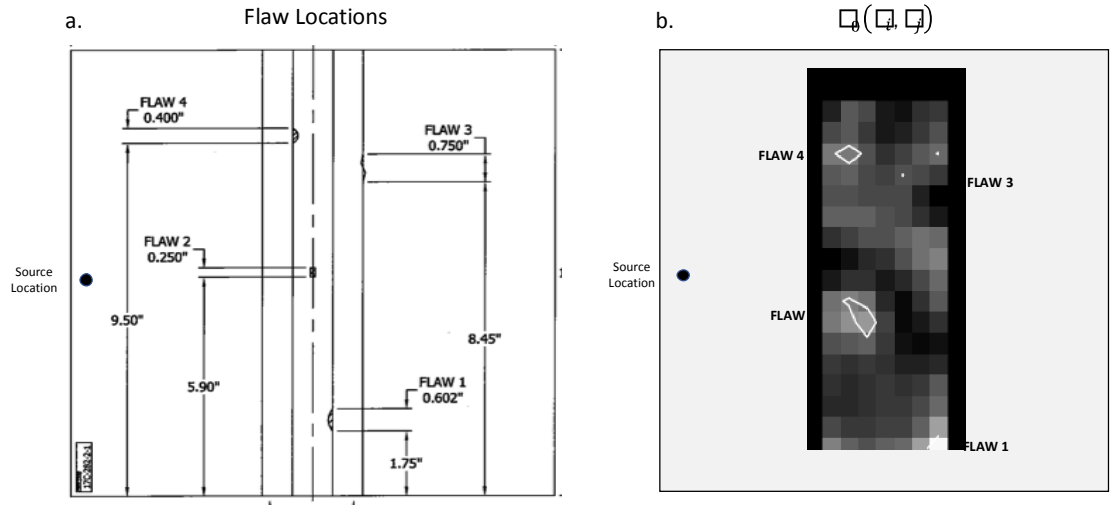

FIG. 10. Shaded region on the left (10.a) defines the scanned region on surface of the plate. The calculated results of the topological energy gradient $G_0(x_i, y_j)$ are shown on the right (10.b). Here the lighter regions with contours show accurate indications of flaws #1, #2 and #4 in the plate. The single contour level set at the median between max and min values of the topological gradient value to improve visualization. Flaw #3 is a crack parallel to the plate boundary and is not resolved completely.

The resulting image and contour map provide a measure of maximum likelihood of 'difference' between the damaged and undamaged regions of the plate. In the test case above the two flaws (#2 and #4) that are most apparent in the $G_0(x_i, y_j)$ and are located in the plane of the plate. The other two flaws #1 and #3 are along the in the rib and the edge of the weld bead respectively. The edge flaw is challenging to resolve as it is a crack parallel to the surface of the plate which have minimal effect on the propagating modes. Detection flaws in the rib can be improved either by scanning on the rib, or by changing the source frequency to promote propagating modes that are more sensitive to surface features.

IV. CONCLUSIONS

An imaging and location technique using acoustic wavefield data sets obtained from scanning a microwave interferometer across a coated steel plate has been presented. With this system, relevant, 10 nm, out-of-plane surface displacements have been detected in the steel plate *through* a 50.8mm (2 in.) viscoelastic layer using a microwave interferometer (MI). The MI presents an alternative approach to existing inspection methods that rely on direct access to the plate weldments through removal of the coating. Frequency-wavenumber analysis and topological energy method have shown promise as possible methods to detect and map thickness variations in coated steel plates as well as flaws in the weldments. Further development is necessary to improve the resolution and robustness of a fieldable design. Excitation of the hull surface poses some engineering challenges. The amplitude of the excitation pulse will also need to be scaled up. Fortunately, guided mode propagation in the hull plates is efficient, and large distances can be traversed by the propagating modes minimizing the number of actuation locations. The interferometer system can be scaled up in-terms of channels where 5-10 interferometers could be integrated into a parallel array that is swept above the surface of the vessel. The swept region would gather data over either side of a weld seam. The entire array, digitizers, and signal conditioning can then be mounted on a large gantry scanner or robotic arm which would follow a pre-programmed contour of the hull. Finally, further refinements in the data processing and imaging algorithms would

include resolution refinement, mapping speed, and data throughput. Flaw characterizing including sizing and void differentiation are also areas where further improvements can be implemented.

VI. ACKNOWLEDGEMENTS

This work was performed under the Navy Metalworking Center, operated by Concurrent Technologies Corporation (CTC), under Contract No. N00014-10-D-0062 to the Office of Naval Research as part of the U.S. Navy Manufacturing Technology Program and under auspices of the U. S. Department of Energy by the, Lawrence Livermore National Laboratory.

REFERENCES

[1] C., Hayes, The ABCs of non-destructive weld inspection, Welding Journal, May 19 1997.

[2] M. Jung, B., Park, S.,Shin, PAUT-based defect detection method for submarine pressure hulls, International Journal of Naval Architecture, March 2018, p153-169.

[3] J., Rose, *Ultrasonic Waves in Solid Media*, Cambridge University Press, Cambridge CB2 2RU, UK, (1999).

[4] M., Ruzzene, Frequency-wavenumber domain filtering for improved damage visualization, Smart Mater. and Struct. **16** (2007) 2116-2129.

[5] T., Micheals, J., Michaels, M., Ruzzene, Frequency-wavenumber domain analysis of guided wavefields, Ultrasonics 51 (2010).

[6] S. Rodriguez, P., Sahuguet, V., Gibait, X., Jacob, Fast topological imaging, Ultrasonics 52 (2012), p1010-1012.

[7] J., D., Achenbach, *Wave Propagation in Elastic Solids*, North-Holland Press, Elsevier Scientific Publishing (1991).

[8] D., Chimenti, Guided waves in plates and their use in material characterization, Appl. Mech. Rev., vol. 50, no. 5, May 1997.

[9] W.H., Steel, I*nterferometry*, Cambridge University Press, (1983).

[10] I. Woodhouse, I*ntroduction to microwave remote sensing*, CRC Press, Taylor and Francis Group, Boca Raton, Fl, 2006.

[11] C., Nguyen, S., Kim, T*heory, Analysis and design of RF interferometric Sensors*, Springer Briefs in Physics, Springer Publishing, ISSN 2191-5423.

[12] J.S Martin, D. J. Fenneman, F.Codron, P., H., Rogers, W. R. Scott G., D., Larsen, and G.S. McCall II, Ultrasonic Displacement Sensor for Seismic Detection of Buried Landmines, Annual International Detection and Remediation Technologies for Mines and Minelike Targets VII, Proceedings of the SPIE vol. 4742 (2002).

[13] W., R., Moore, Foundations of Mechanical Accuracy, The Moore Special Tool Company, Libr. Congr. No. 73-127307, 800 Union Ave. Bridgeport, CT, (1970).

[14] S., Garreau, Topological asymptotic for PDE systems: the elastic case, SAIM L. Contrl. Optim.,39(6), (2001),1756-1778.

[15] E., Lubeigt, S., Mehsah, F.,Baque, Topological imaging in bounded elastic media, Ultrasonics 76 (2017), p147-153.

[16] V., Gibait, P., Sahuget, Waveguide imaging through time domain topological energy, Ultrasonics, 50 (2010) 172-179.

[17] N., Dominguez, V., Gibait, E., Esquerre, Time domain topological gradient and time reversal analogy: an inverse method for ultrasonic target detection, Wave Motion, 42 (2005), p 31-52.

[18] A., Mubashir, J., H., McClellan, W., R., Scott, Multichannel analysis of surface waves, IEEE, 37th Asilomar conference on signals, systems, and computers, (2003), p 771-777.

[19] T., Hayashi, Defect Imaging for plate-like structures using a diffuse field', J. Acoust. Soc. Am., 143(4) (2018), p260-264.

[20] D., Alleyne, and P., Cawley, A two-dimensional Fourier transform method for the measurement of propagating multimode signals, The Journal of the Acoustical Society of America 89, 1159 (1991);

[21] A., Behboodian, W. R., Scott, J. H., McCellan, Signal Processing of surface waves for localization of buried Land Mines", IEEE (1999).

[22] N., Dominguez, V., Gibait, Non-destructive imaging using time domain topological energy methods, Ultrasonics, 50 (2010), p 367-372.

[23] K. F. Graff, Wave Motion in Elastic Solids, (Ohio State U P, Columbus, 1975), pp. 274.

[24] COMSOL v 5.3.1, COMSOL, Inc. 100 District Avenue, Burlington, MA 01803 USA.

[22] M., Born and E., Wolf, *Principles of Optic*s 7th edition, Cambridge University Press, Cambridge,2001, p702-703.

Figure	Caption
1	Elastic-microwave interferometric based measurement approach. Here the interferometer measures the total out-of-plane displacement on the upper surface of the plate. Flaws will generate localized changes in the elastic field due to propagating and non-propagating modes.
2	Basic operational components of the W-Band homodyne Microwave Interferometer (reflectometer). Here, w(t) is the time-varying acoustic surface displacement, D, is the standoff path length, λ, is the wavelength of the transmitted signal. Reference and received signals are mixed to produce the in-phase and quadrature results I(t) and Q(t) respectively. The quadrature signals are processed and combined to obtain an estimate of w(t) given by Eq. 5.
3	Scanning set up for the coated steel plates. The 2 in. coating on the upper surface has been omitted for clarity. The microwave interferometer (MI) is held stationary in the spindle of a vertical machine mill. The plate is positioned under the horn at each of the scan locations (gray dots) by adjusting the x-y travel on the mill bed. The Guided modes in the plate are generated by a piezoelectric shaker driven by a sinusoidal windowed pulse.
4	The array plot on the right is a typical 1D wavefield data set with waveform amplitudes normalized. The shaker source location (black) is constant for all scan locations (red). The displacement measurements are recorded through the coating. The outlines show the details of the five thinned regions, each has a different depth and edge profile.
5.	Process of determining a local wavenumber estimate from a region of interest (roi) subset. **a.** A slice of the spato-temporal $\widehat{W}^E$ data is chosen at ω_o. **b**. A 3x3 region centered at (x,y) is selected and a 2D spatial transform is calculated. **c.** The maximum absolute value of a 2D spatial transform in the 3x3 widow centered at (x_i,y_i) is proportional to an estimate of the local wavenumber $k'(x_i,y_i,\omega_o)$. The wavenumber estimate is repeated at each scan location using the selected roi.
6.	The shaded region contains the locus of common group velocities that can be utilizes as a baseline to perform differencing operations on the phase velocities to indicate thickness variations. Here the perturbed phase speed is calculated by $c_{ph}^1(x_i, y_j, (fd)_1)$; $(fd)_1 = (fd)_o + \Delta(fd)$ where $(fd)_o$ is the chosen at the locus of common group velocities and $\Delta(fd)$ is a small perturbation from the locus.
7.	In this example the, image on the left shows the scanned region of the plate and the thinned regions. The depth of the thinned regions ranges from 1/32 to ½ of an inch. Here, the thinnest region of the plate (largest deviation from nominal) has been normalized to unity. Darker regions correspond to less thinning with black corresponding to no thinning. The ½ inch deep region in the upper left is clearly visible, as is the center region at 3/32" both show a significant difference from the non-thinned regions of the plate. Note, the coating has been omitted for clarity in the image on the left.
8	Imaging feature shapes using local wavenumber estimates. The data subset on the left has been used to generate the contour map on the right. The source location is shown

	in green. While the contour magnitudes indicate the backward 'L' shape, the resolution is low due to the coarse spatial sampling. Again, the coating has been omitted for clarity in the image on the left, the wavenumber contours on the right were obtained from microwave interferometer measurements *through* the poly-urethane coating.
9	Process for determining flaws in weldments using a topological energy method, the pristine data $u_o(x, y, z_o, t)$ is determined from a 3D finite element time domain model and the adjoint field $v_o(x, y, z_o, t)$ is determined from the time-reversed *difference* between the pristine model and experimental measurements.
10	Imaging results of the topological energy gradient for the shaded region on the left. The scan map on the left shows the location of the wavefield data set (red circles). The source location is shown in green. The gradient map, $G_0(x_i, y_j)$ on the right clearly shows two of the reported flaws in the plate, #2 and #4.